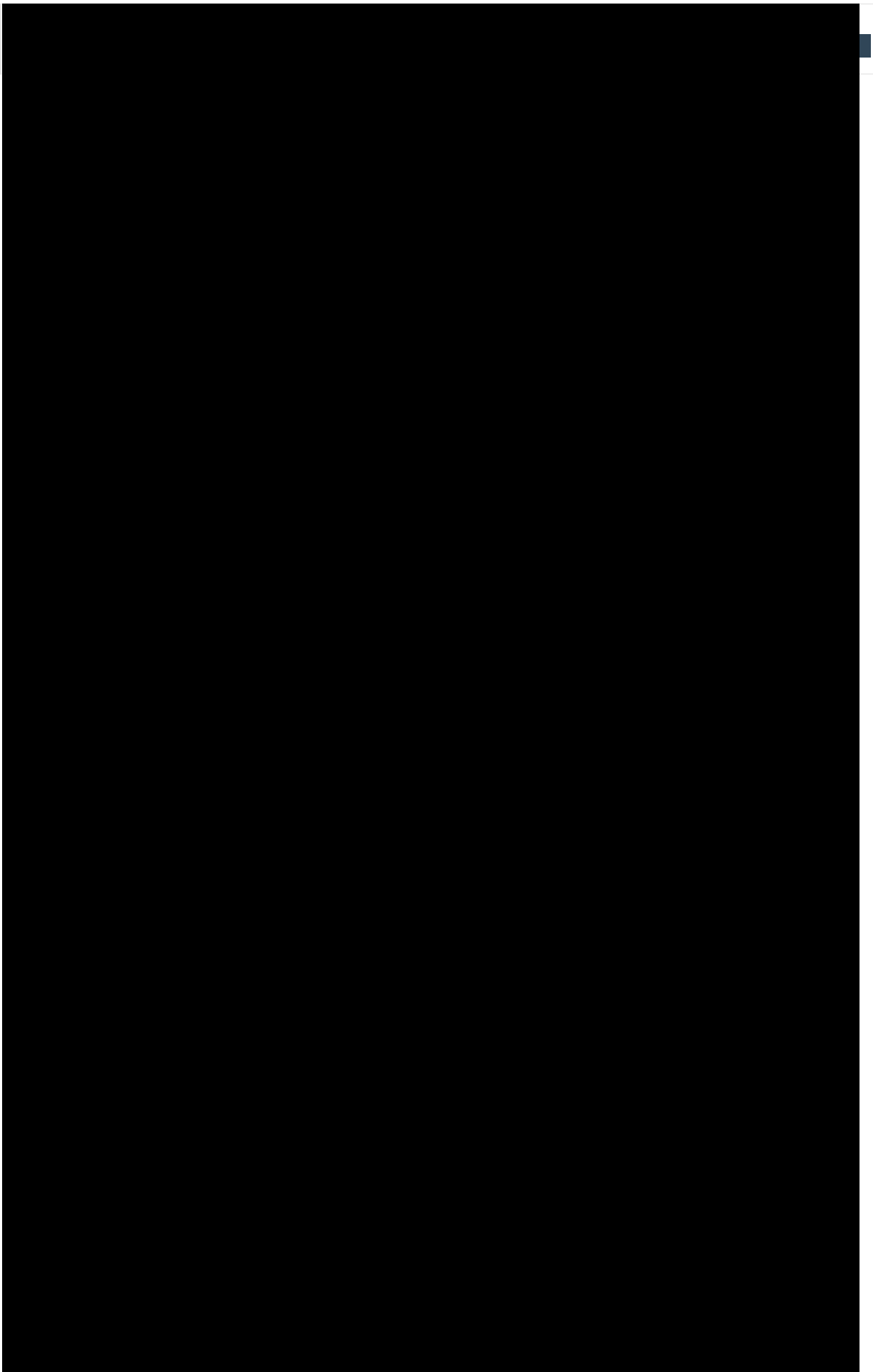

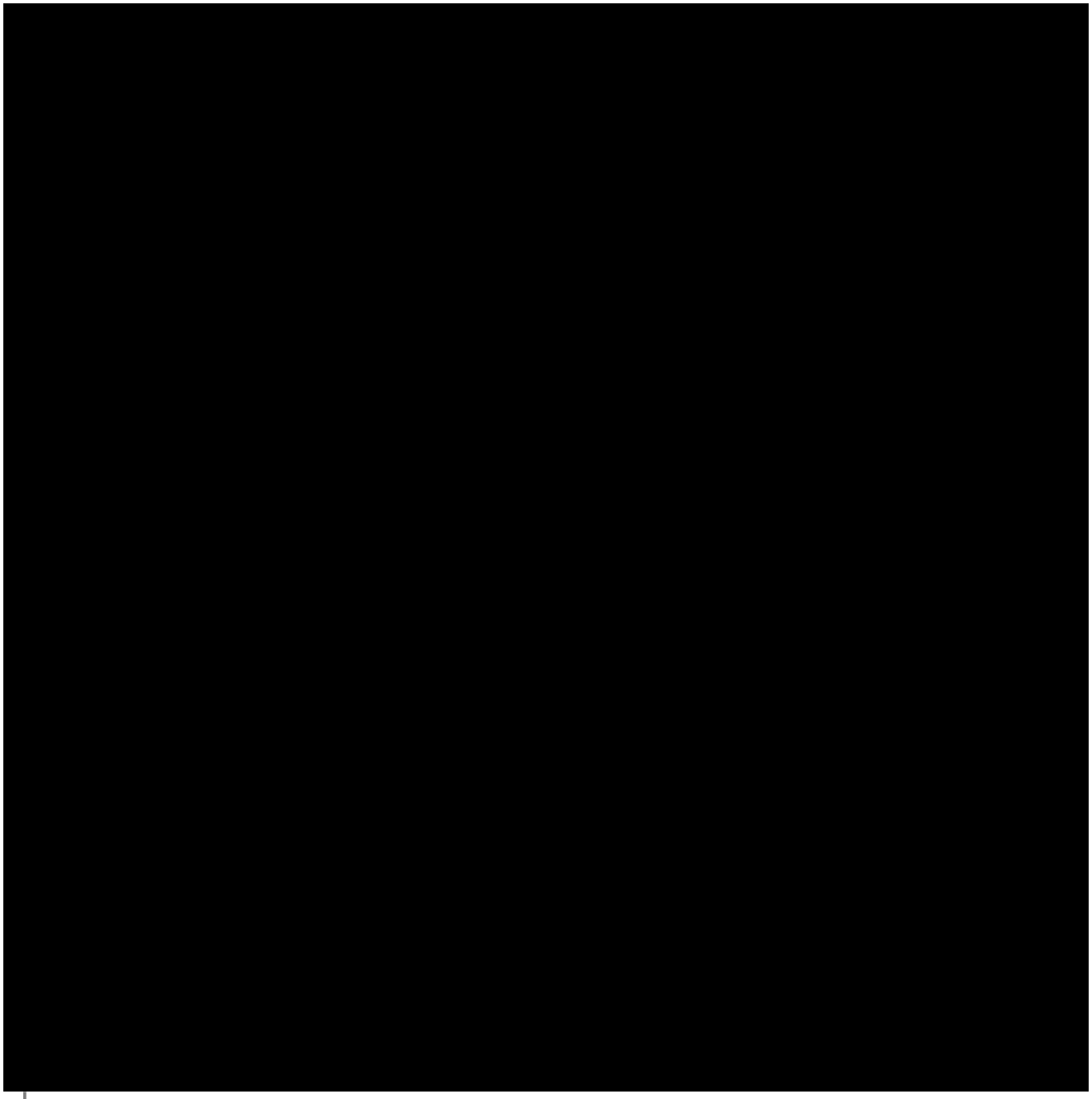

Article

Nanoscale imaging of mobile carriers and trapped charges in delta doped silicon p–n junctions

Georg Gramse, [1✉,2]

Email georg.gramse@jku.at

Alexander Kölker, [3,4]

Tomas Skeren, [5]

Taylor J. Z. Stock, [3]

Gabriel Aeppli, [6,7,8]

Ferry Kienberger, [2]

Andreas Fuhrer, [5]

Neil J. Curson, [3,4]

[1] Johannes Kepler University, Biophysics Institute, Linz, Austria

[2] Keysight Technologies Austria GmbH, Keysight Labs, Linz, Austria

[3] London Centre of Nanotechnology, UCL, London, UK

[4] Department of Electronic and Electrical Engineering, UCL, London, UK

[5] IBM Research – Zurich, Rüschlikon, Switzerland

[6] ETH, Zurich, Switzerland

[7] EPFL, Lausanne, Switzerland

[8] Paul Scherrer Institut, Villigen, Switzerland

Received: 19 December 2019 / Accepted: 30 June 2020

Abstract

Integrated circuits and certain silicon-based quantum devices require the precise positioning of dopant nanostructures, and hydrogen resist lithography can be used to fabricate such structures at the atomic-scale limit. However, there is no single technique capable of measuring the three-dimensional location and electrical characteristics of these dopant nanostructures, as well

as the charge dynamics of carriers and trapped charges in their vicinity. Here, we show that broadband electrostatic force microscopy can be used for non-destructive carrier profiling of atomically thin n-type (phosphorus) and p-type (boron) dopant layers in silicon, and their resulting p–n junctions. The probe has a lateral resolution of 10 nm and a vertical resolution of 0.5 nm, and detects the capacitive signature of subsurface charges in a broad 1 kHz to 10 GHz frequency range. This allows the bias-dependent charge dynamics of free electrons in conducting channels and trapped charges in oxide–silicon interfaces to be investigated.

Editor's Summary

Broadband electrostatic force microscopy can be used to non-destructively image n-type and p-type dopant layers in silicon devices with a lateral resolution of 10 nm and a vertical resolution of 0.5 nm.

These authors contributed equally: Alexander Kölker, Tomas Skeren.

Main

The patterned doping of silicon at the nanometre scale, for both classical and quantum applications, brings new diagnostic challenges. For example, the visualization and electrical characterization of dopant structures within a single transistor is difficult due to the reduced transistor size in current complementary metal–oxide–semiconductor (CMOS) technology. This has serious implications for quality control and security in integrated circuit (IC) manufacturing, where tampering of the local dopant profile has been shown to compromise IC integrity[1]. Thus, the development of techniques that can overcome current diagnostic limitations is essential[2, 3, 4]. In particular, the development of a technique capable of non-destructive, nanoscale measurements, as well as quantitative electrical characterization, would be valuable for both IC failure analysis[5] and the creation of quantum architectures[6] based on quantum confined dopant nanostructures.

AQ1

AQ2

AQ3

AQ4

Using scanning tunnelling microscopy (STM) hydrogen resist lithography, both acceptors[7] and donors[8] can be patterned with atomic resolution into dopant nanostructures[6] such as sheets[9], wires[10] and dots[11]. This atomic-resolution doping has also been implemented in three-dimensional (3D) structures[12] and can be integrated into a CMOS platform[13]. However, STM is relatively insensitive to the subsurface[14] when used to measure such structures, although scanning microwave microscopy (SMM) can be used non-destructively to determine the 3D location of structures once they are buried within the silicon wafer[15].

In this Article, we show that donor–acceptor interface nanostructures can be fabricated by STM and then quantitatively characterized using broadband electrostatic force microscopy (bb-EFM). This technique can sense the impedance gradient under different local biasing conditions across a broad frequency range from 1 kHz to 10 GHz, and offers a factor of two improvement in lateral resolution and a factor of five improvement in sensitivity compared with SMM. Quantitative finite-element simulations, using a semiconductor drift-diffusion model, allow us to extract the vertical distribution and polarity of the carriers with high confidence and without the need for a special calibration sample. Furthermore, bb-EFM measurements made at varying frequencies allow us to estimate the density of oxide-interface trap states, which determine the performance of the final device[16].

Unlike destructive imaging techniques—such as transmission electron microscopy (TEM)[17], focused ion beam scanning electron microscopy[18], secondary ion mass spectrometry (SIMS)[19], atom probe tomography (APT) or scanning spreading resistance microscopy (SSRM)[20]—which require milled, bevelled or cross-sectioned samples, EFM is non-destructive. The technique can also be performed in an ambient environment using a standard atomic force microscope (AFM) with a lock-in amplifier and a signal generator. In addition, measurements are performed in tapping mode, which provides an important advantage over SMM where the best resolution requires the more invasive contact mode.

bb-EFM

The bb-EFM set-up is shown in Fig. 1 and its operation is fully explained in the

Methods. In brief, a signal generator is connected to a conducting AFM probe. The electric potential V between the probe and the sample deflects the cantilever under an electrostatic force F_{es} following the relation

$$F_{es} = \frac{1}{2}\frac{dC^*}{dz}V^2 \quad (1)$$

The complex capacitance gradient dC^*/dz, which we denote C', gives information on the local impedance below the tip and thus on the presence of dopants (changes of C' relative to an offset C'_0 are denoted $\Delta C' = C' - C'_0$). Equation (1) simply states that the force is the derivative with respect to the probe–sample distance z of the energy CV^2 stored by the capacitor. For the particularly simple case of a parallel-plate capacitor model, with plates of area A separated by a distance z, $C = A\varepsilon/z$. For a fixed value of A and a dielectric permittivity ε that is independent of z, $C' = -A\varepsilon/z^2$. Thus, for given values of A and ε we can determine the distance z between the surface of a medium and a conducting plane produced, for example, by a delta doping layer below the surface. When applying an amplitude-modulated electric field $V_{ac} = V_{ac,0}\cos(2\pi f_{mod}t)\cos(2\pi f_{carrier}t)$ with a carrier frequency $f_{carrier}$ and amplitude $V_{ac,0}$, we detect, with the lock-in amplifier, a cantilever oscillation at a frequency f_{mod}. The electrostatic force producing this deflection is a measure of the local tip–sample capacitance gradient[~~20~~][21]

$$F_{es,\omega\,mod} = 1/4\,|C'(V_{bias}, f_{carrier}, z)|\,V_{ac,0}^2 \quad (2)$$

$F_{es,\omega mod}$ can then be studied as a function of V_{bias} and $f_{carrier}$. Note that $f_{carrier}$ is set independently from f_{mod} and is not influenced by cantilever mechanics[21]. As a result, the frequency range available to bb-EFM (1 kHz–10 GHz) is orders of magnitude larger than those typically used in current-sensing techniques like impedance microscopy[22, 23] (<10 MHz), scanning capacitance microscopy[24] (1 MHz), scanning nonlinear dielectric microscopy[25] (1 GHz) or SMM[~~15~~26] [15](1–20 GHz), all of which rely on a very narrowband matching of the electronic detection circuitry to achieve the required electrical sensitivity. Additionally, we note that the capacitance gradient C' signal offers more spatially localized information[27, 28], and an improved electrical sensitivity, limited only by the thermal noise of the cantilever[29].

Fig. 1

bb-EFM for 3D dopant profiling.

The electrostatic force (change of capacitance derivative $\Delta C'(z)$) on a conductive AFM probe is measured to obtain the 2D footprint of a buried dopant layer with nanometre lateral resolution. The doping profile in the vertical dimension is obtained by probing $\Delta C'$ as a function of sample bias V_{bias}, probe–sample distance z and measurement frequency f. The finite element model (FEM) shown on the bottom right is used to extract quantitative information. For frequency-dependent measurements, a signal generator delivers an amplitude-modulated signal to the AFM probe with a fixed kHz modulation frequency and a carrier frequency f_{carrier} between 100 kHz and 10 GHz. The induced electrostatic force is recovered through the lock-in amplifier (LIA) by direct amplitude modulation. Electrostatic force images are acquired together with topography in tapping mode.

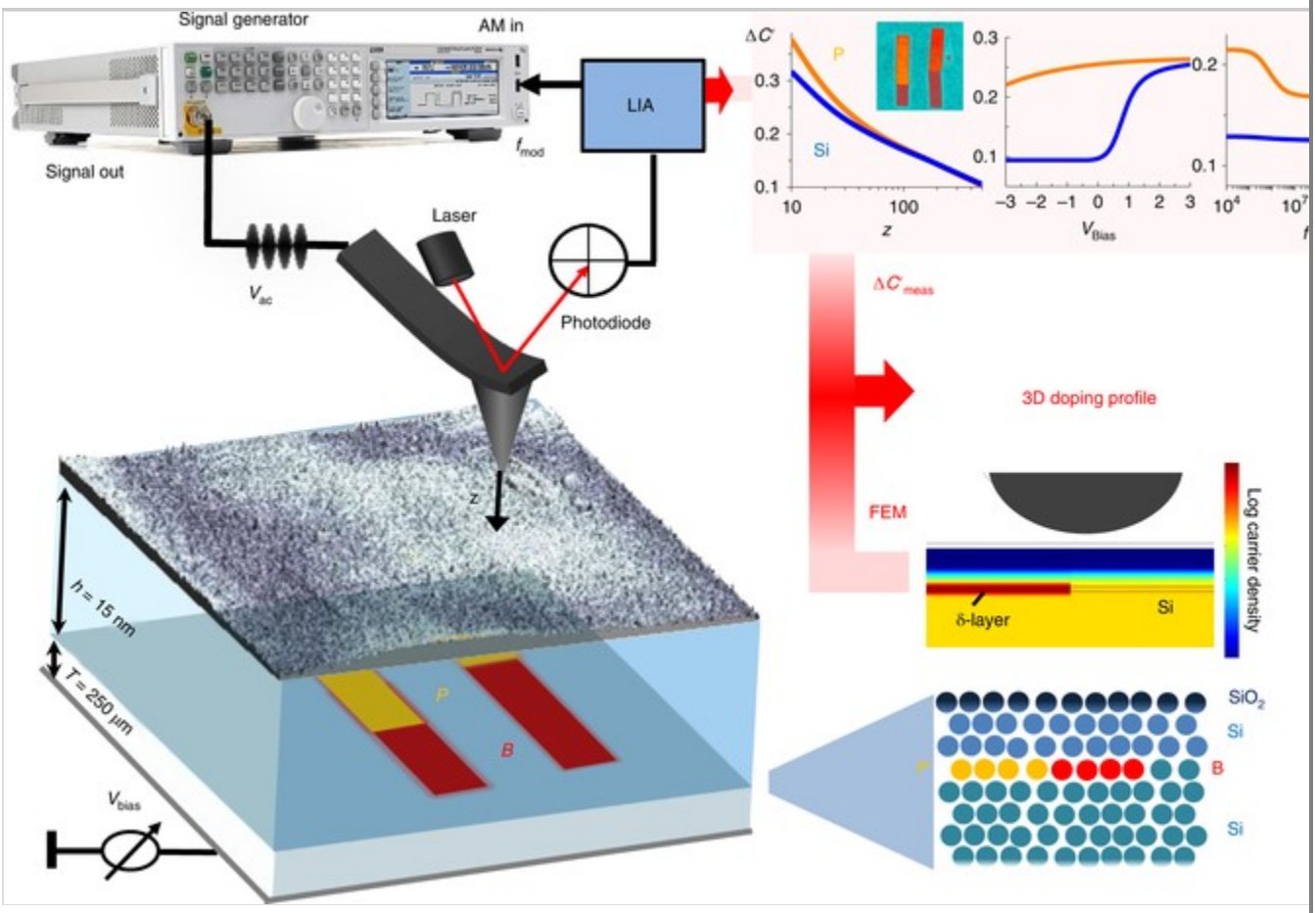

AQ5

Subsurface imaging and lateral resolution

Structures consisting of atomic layers (‘δ-layers’) of B and P were patterned onto

a Si(100) surface and subsequently encapsulated by a 15-nm-thick epitaxial Si layer, as detailed in the Methods. Figure 1 shows the resulting surface topography. In Fig. 2a, the same AFM tapping mode topography measurement is overlaid with simultaneously acquired EFM data. In Fig. 1, the surface topography is extremely flat (average roughness of <1 nm) and gives virtually no information about the dopant structure location. The encapsulation was therefore successful, and the applied electric field has no measurable impact on the topographic image. However, the superimposed electrostatic $\Delta C'$ image in Fig. 2a displays an excellent contrast between the spatially averaged values of $\Delta C'_{\mathrm{P}} = 0.40$ aF nm^{-1} and $\Delta C'_{\mathrm{B}} = 0.25$ aF nm^{-1}, measured above the nanostructured P and B bars, and the surrounding Si substrate background. This corresponds to a ~~S/N~~signal-to-noise ratio (SNR) of $\Delta C'_{\mathrm{P}}/C'_{\mathrm{Noise}} = 12$ and $\Delta C'_{\mathrm{B}}/C'_{\mathrm{Noise}} = 7$ (see lower profile line in Fig. 2c), six times better than SMM where we obtained $\Delta C'_{\mathrm{P}}/C'_{\mathrm{Noise}} = 2$ with an AFM probe of comparable sharpness[15]. One curious observation from Fig. 2a, explained in detail in the following section, is that the $\Delta C'$ signal intensity from the B δ-layers is lower than for P δ-layers.

Fig. 2

Patterned B and P δ-layer structure buried $h = 15$ nm below the surface.

a, Overlay of AFM topography and $\Delta C'(z)$ image. **b**, $\Delta C'(z)$ image of B resolution test patterns (the stripes have a constant gap of 60 nm and decreasing width from the left to the right: 2×32 nm, 2×16 nm, 3×8 nm, 5×4 nm). **c**, Corresponding $\Delta C'(z)$ profile lines. Red lines show fitting with a logistic function as detailed in the text. The PtSi-FM tips are from NanoSensors (Germany) and have a nominal tip radius of $R = 30$ nm ($V_{\mathrm{bias}} = 0$ V, $V_{\mathrm{ac}} = 1.5$ V, $f_{\mathrm{carrier}} = 242$ kHz).

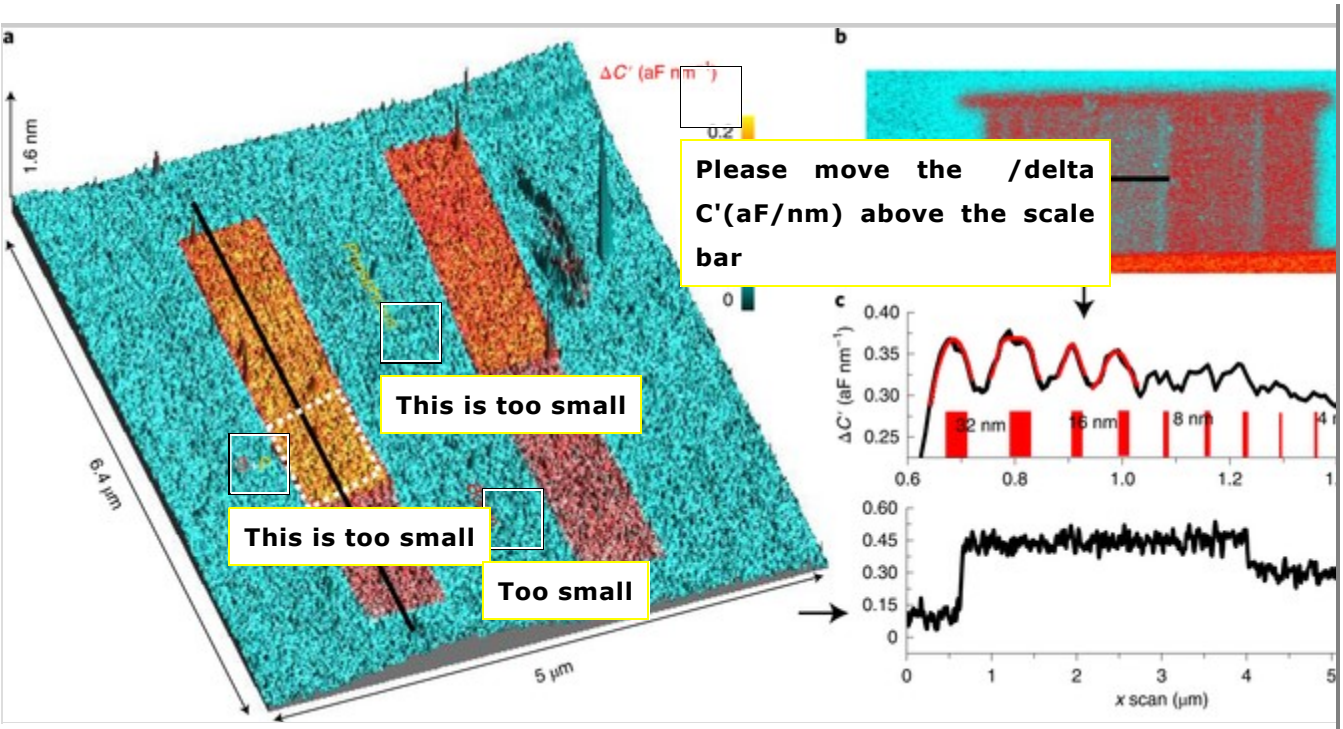

AQ6

The lateral resolution of the EFM was estimated using patterned B bars of decreasing widths, separated by constant gaps of ~60 nm, as displayed in Fig. 2b, and Extended Data Fig. 1 showing STM measurements prior to encapsulation. The first two sets of two bars with widths of 32 nm and 16 nm are easily resolved and a constant level is reached in the middle of each bar. However, the following bars with widths of 2 × 8 nm and 5 × 4 nm are only resolved as peaks, while thinner bars (that is, 4 nm and 2 nm) are not resolved at all. The line patterns on the right half of Fig. 2b, with 30- and 15-nm gaps, are nearly unresolved. Fitting a sum of two logistic functions $f_{\mathrm{logis}}(x) = A\left(1+\mathrm{e}^{-(x-x_0)/\delta}\right)^{-1} - A\left(1+\mathrm{e}^{-(x-x_1)/\delta}\right)^{-1}$ to the edges of the 32-nm and 16-nm bars, we calculate a lateral resolution of $2\delta = 10 \pm 5$ nm. This value is surprisingly good for a pattern buried 15 nm below the surface and is approximately five times better than the lateral resolution achieved by SMM (cf. $2\delta_{\mathrm{SMM}} = 55$ nm)[15] using similar samples and tip–apex radii ($R_{\mathrm{apex,EFM}} = 26.4 \pm 0.2$ nm and $R_{\mathrm{apex,SMM}} = 20 \pm 1$ nm[15]; for tip calibration see Extended Data Fig. 2c and Methods). A direct comparison of bb-EFM and SMM on the same P patterned sample, presented in Extended Data Figs. 2 and 3, confirms these EFM results ($2\delta = 13 \pm 2$ nm) and demonstrates that bb-EFM can clearly distinguish bars separated by 30 nm, while this is impossible with SMM[15]. We expect the

various measurement parameters to affect lateral resolution differently in the force-sensing (C') and current-sensing (C) techniques. Modelling in Extended Data Fig. 4 shows that, while the tip radius has little impact here, the advantage of the C' measurement increases at larger tip–sample distance. In both models and experiments, the C' measurement exhibits maxima in both lateral resolution and dopant contrast at a measurement frequency of ~10–100 MHz (Extended Data Figs. 4 and 5).

Quantitative dopant profiling

In addition to determining the lateral position of a patterned δ-layer, it is also important to measure its vertical position and electrical characteristics. In particular, the carrier sign and concentration are key determinants of the operational behaviour of a device. Figure 3c describes the bb-EFM contrast mechanism with a simplified equivalent circuit. For Si regions without a δ-layer, an effective capacitance (air + oxide + depletion layer) in series with the bulk resistance is formed below the tip. With the δ-layer present, this buried, highly conductive sheet acts as a 2D electron gas (2DEG) capacitively coupled to the tip and bulk substrate in series. The AFM probe apex diameter R and distance z from the surface define the local field penetration depth below the surface and the probed sample volume. Application of a d.c. bias between sample and tip attracts or repels carriers depending on their sign, and modulates the depletion capacitance under the tip depending on their concentration[30]. Additionally, in the δ-layer region, we assume that the bias modulates the occupation of δ-layer bands and therefore the 2DEG sheet resistance. Measuring C' as a function of tip bias V_{bias} and the tip–sample distance z should therefore allow us to determine the carrier type and vertical carrier concentration profile.

Fig. 3

Quantitative dopant profiling of a P patterned sample.

a, Left: C' image of a test sample acquired at $f_{\mathrm{carrier}} = 1$ GHz, $z = 24$ nm and $V_{\mathrm{bias}} = 0$ V. Right: schematic cross-section of the 3D test sample. **b**, Normalized capacitance versus voltage curves acquired at the locations indicated in **a**. Black solid lines represent the best fits of FEM-calculated C' curves to experimental data as detailed in the text ($f_{\mathrm{carrier}} = 1$ GHz, $z = 22$ nm). **c**, Simplified equivalent circuit model (left) of the P δ-layer (where R_x is the bulk resistance, R_{s} is the δ-layer sheet

resistance and h is the depth of the δ-layer below the surface) and FEM of the AFM tip 10 nm above a surface containing a P δ-layer (the potential distribution is shown in colours). The conduction band energy minus the Fermi energy level is plotted along the symmetry axis for dopant concentration of 3×10^{18} cm^{-3} (dotted lines) and 3×10^{21} cm^{-3} (solid lines) for different biases (3 V, red; 0 V, orange; −3 V, black). **d**, Capacitance approach curves and FEM fitting ($f_{carrier} = 1$ GHz, $V_{bias} = 0$ V). Symbols are colour-coded as in the schematic to the right of **a**.

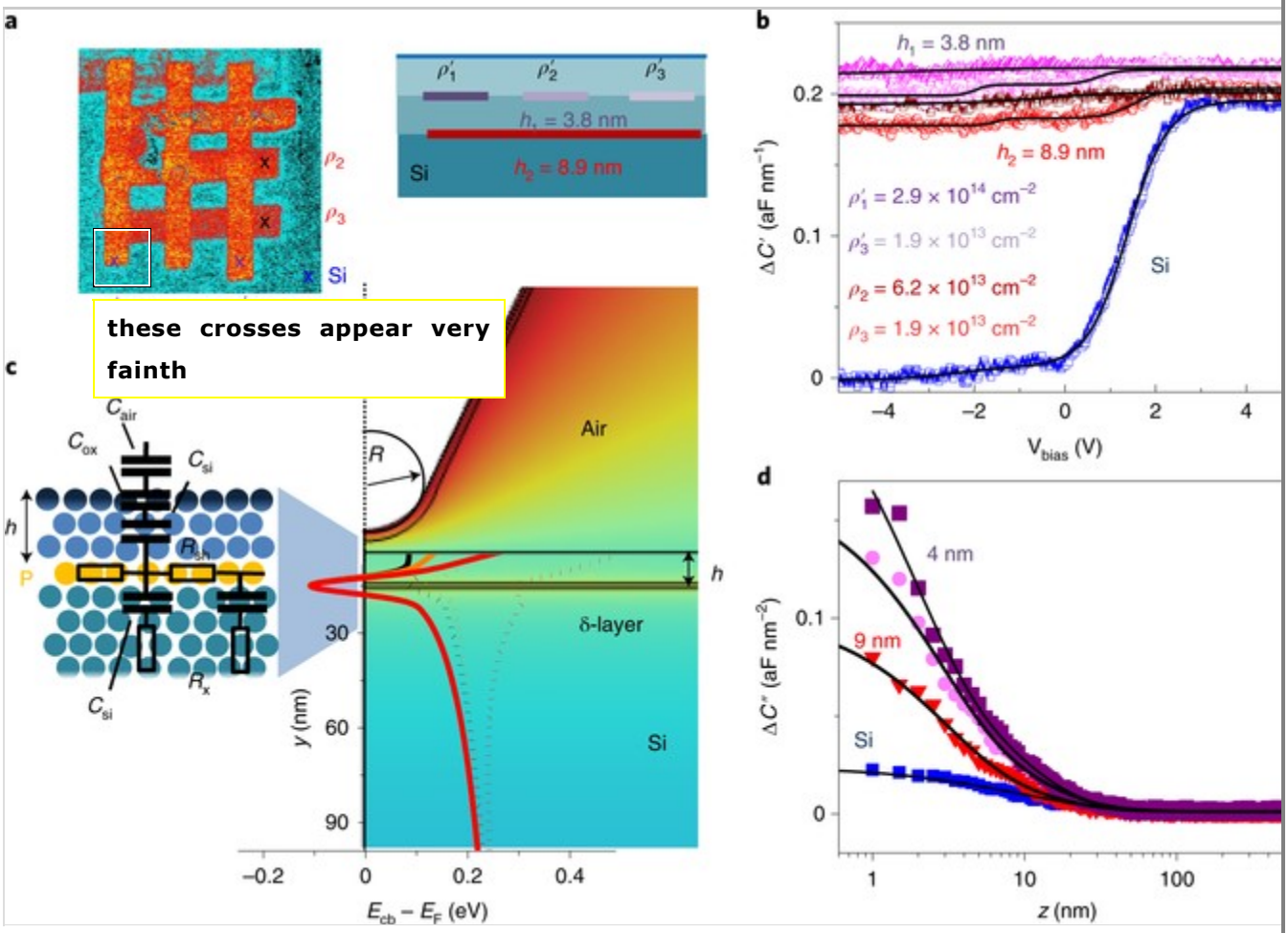

We show this quantification for a test sample containing six P δ-layer bars at two different depths and three different, independently verified, dopant sheet densities ($\rho_{sh,1} = (2.87 \pm 0.03) \times 10^{14}$ cm^{-2}, $\rho_{sh,2} = (6.23 \pm 0.03) \times 10^{13}$ cm^{-2} and $\rho_{sh,3} = (1.86 \pm 0.03) \times 10^{13}$ cm^{-2})[15] within an As-doped (3×10^{14} cm^{-3}) Si wafer. Assuming a Gaussian δ-layer distribution with $\sigma = 1.5$ nm, this corresponds to a dopant concentration peak value of $\rho = \rho_{sh}\sigma^{-1}(2\pi)^{-1/2}$, giving $\rho_1 = (7.63 \pm 0.08) \times 10^{20}$ cm^{-3}, $\rho_2 = (1.66 \pm 0.08) \times 10^{20}$ cm^{-3} and $\rho_3 = (0.49 \pm 0.08)$

$\times 10^{20}$ cm^{-3}. The P δ-layers are structured as sketched in Fig. 3a, with their concentration maximum located at depths of $h_{nom} = (3.8 \pm 0.1)$ nm and $h_{nom} = (8.9 \pm 0.1)$ nm, as confirmed by SIMS measurements[15]. Although the topography of the test sample is flat (Supplementary Fig. 2), the EFM image in Fig. 3a clearly visualizes the presence of the patterned bars. To extract the dopant profile we acquired $C'(V_{bias})$ and $C'(z)$ curves at different positions on the sample. The Si $C'(V_{bias})$ curve in Fig. 3b, acquired over an area with no δ-layer, resembles a classical high-frequency capacitance versus voltage curve for n-type dopants, where we find electron accumulation with high capacitance for high positive biases, depletion with reduced capacitance between 0 and 2 V, and a further decrease of the capacitance in inversion. Acquiring the same curve on the P stripes, we find the C' difference between accumulation and depletion/inversion is much lower compared to Si. Interestingly, the P bars patterned with a low dopant density exhibit two decays, while the highly doped bars, at both 4 nm and 9 nm below the surface, show only one. This is again in agreement with the picture of a highly doped δ-layer with low R_{sh} acting as an electrically floating metallic plane in which the measured C' is dominated by the geometrical capacitance between the probe and δ-layer. An applied d.c. bias modulates only the small epitaxial Si region between the probe apex and δ-layer, which has little impact on the overall signal, and results in a single decay in the $C'(V)$ curve (Extended Data Fig. 6b). For a low-doped δ-layer, the sheet resistance is high and the geometrical capacitance plays a minor role, and a simpler, 1D picture of a metal–insulator–semiconductor structure applies. Here, the depletion capacitance $C_{si}(V)$ dominates while the increasingly negative applied bias pushes the depletion layer deeper into the substrate. The resulting decays in the $C'(V)$ curve represent variations in the vertical dopant level (Extended Data Fig. 6).

The experimental $C'(z)$ approach curves in Fig. 3d indicate that the δ-layers can only be sensed when the AFM probe is located very close to the surface ($z < 30$ nm). For distances above 50 nm, most of the applied potential drops off in the air gap between tip and sample, and $C'(z)$ curves acquired with and without δ-layers practically overlap. Consequently, it is critical to carry out the electrical characterization of the δ-layers with low tapping amplitudes. With our microscope, using PtSi-FM probes, amplitudes between 5 nm and 20 nm were optimal.

To quantitatively extract the active dopant profile from our measurements, we developed an FEM that captures the specific geometry and boundary conditions of the experimental arrangement and solves for the potential (shown in Fig. 3c) and carrier distribution (for details see Methods). Using this model, we calculate $C'(z,V,f,h,\rho)$ for a large range of values of the h and ρ parameters. Best-fit h and ρ values for the measured δ-layer are then extracted through comparison of the calculated and experimentally measured C' values.

This model is significantly more realistic than previous electrostatics-based FEM models[15], and allows us to interpret bias-dependent measurements. We note that the simulation is fully based on a drift-diffusion model and therefore cannot be used to explain quantum confinement effects that might be especially relevant at low temperatures where medium- and low-doped silicon is not conductive. However, for measurements at ambient conditions, the doped silicon semiconductor model used here offers a good approximation. This can be seen from the calculated conduction band profile of a P δ-layer shown in the inset of Fig. 3c. Here, we indeed observe that only for high dopant densities (3×10^{21} cm^{-3}, solid lines) does the effective conduction/donor band energy reside below the Fermi level ($E_{CB} - E_F < 0$) and thus act like a floating metallic plane. A bias potential applied either to the tip or the substrate only modifies the energy profile in the silicon above the δ-layer. By contrast, for lower dopant concentrations (3×10^{18} cm^{-3}, dashed lines) the applied bias also modulates the energy profile below the δ-layer.

Finally, for determination of the dopant density profile we calculated $C'(V)$ and $C'(z)$ curves from the FEM model and fit them to the experimental data. For the bare silicon data, the calculated $C'(V)$ curve fits very well, assuming a tip work function[31] of 5.7 eV and a tip radius of $R = 53 \pm 2$ nm, only slightly higher than the manufacturer-specified nominal tip radius. This agreement with simulation for the bare silicon confirms the conceptual viability of the model. Using these fixed values of the tip radius and work function parameters, the dopant density ρ and layer depth h are then extracted from the P δ-layer region measurements. The results are summarized in Table 1. The $C'(V)$ curves allow extraction of dopant concentration with high confidence, while dopant depth h is extracted with lower confidence. The contrary is the case for the $C'(z)$ curves where the dopant depth and concentration are estimated with high and low confidence, respectively.

Indeed, a sensitivity analysis based on the FEM, presented in Supplementary Section 1, confirms this experimental finding. The two datasets complement each other and allow extraction of the 3D dopant profile with overall high confidence. The values obtained for the depths of the top and bottom layers and the maxima of their dopant densities are in good agreement with values obtained independently on non-patterned samples by SIMS and Hall-bar measurements[15, 32], respectively. Thus, in addition to the benefits bb-EFM offers over SMM and other related techniques, these results not only prove that the technique retains the ability to quantitatively determine depth and sheet resistance, but the results in Table 1, in fact, show a factor of two improvement in measurement accuracy compared with SMM[15]. Based on the modelling discussed in the Supplementary Information (Extended Data Fig. 7), the sensitivity of the bb-EFM technique to buried dopants is expected to be strongest at medium to high doping levels (>5 × 10^{16} cm^{-3}), while low and medium dopant densities lead to a decrease in lateral resolution.

Table 1

Doping profiling results on a 3D P sample obtained from FEM calculations and experimental data

AQ7

SIMS	**ρ (10^{20} cm^{-3})**		***h* (nm)**	
ρ (10^{20} cm^{-3})/*h* (nm)	***C*′(*V*)**	***C*′(*z*)**	***C*′(*V*)**	***C*′(*z*)**
7.6 ± 0.1/3.8	7 ± 2	9 ± 8	3 ± 1	4.3 ± 0.4
0.5 ± 0.1/3.8	0.5 ± 0.2	0.5 ± 0.5	5 ± 1	4.1 ± 0.7
1.7 ± 0.1/8.9	1.7 ± 0.9	5 ± 4	8 ± 2	8.5 ± 0.5
0.5 ± 0.1/8.9	0.7 ± 0.2	–	9 ± 2	–
The results correspond to fittings shown in Fig. 3 for a P δ-layer at *h* = 15 nm in Si with a 3 × 10^{14} cm^{-3} As background doped~~ed~~ing.				

Electrical characteristics of carrier types and traps

In addition to the local carrier profile, the carrier type can also be inferred from the *C*′(*V*) curve. As shown in Fig. 4a and Extended Data Fig. 8, application of a bias to the tip or the substrate mainly modulates the carrier distribution between

the surface and the highly doped δ-layer, while the electron concentration in the δ-layer and below changes only slightly. When negative voltages are applied to n-type δ-doping, electrons above the δ-layer are repelled from the surface, while for positive voltages they are attracted towards the surface. In contrast, for the $C'(V)$ curve obtained on the p-type B pattern, C' rises for negative voltages where the holes are attracted towards the surface and falls for positive bias where the holes are repelled (Fig. 4c). The $C'(V)$ curve is therefore essential to identify the carrier type and complements the C' image. Note that we measured the $C'(V)$ curves at 1 MHz to remove any capacitive contribution from interface traps, which become visible at lower frequencies, as discussed in the following.

Fig. 4

Dynamics and interface traps.

a, Simulated carrier distribution (electrons) for a bias of −3 V and +3 V. Below: an equivalent circuit model that also accounts for traps in the oxide–semiconductor interface. **b**, C' image showing the locations where $C'(V,f)$ experiments were carried out. **c**, $C'(V)$ spectra acquired at 1 MHz, at the positions indicated in **b**. Three sweeps were averaged. Single data traces are provided in Extended Data Fig. 10, showing the reproducibility achieved. **d**, Calculated interface trap density as detailed in the text. **e**, Frequency-dependent $C'(V)$ spectra on the four sample locations indicated in **b**. The y axes in these contour plots show the measurement frequency with logarithmic spacing from 1 kHz to 1 MHz. **f**, Normalized $C'(f)$ spectra measured over seven orders of magnitude at $V_{\mathrm{bias}} = 0$ V (normalization by C'_{bg} is detailed in the Experimental section). Dashed lines correspond to fitting with calculated $C'(f)$ from FEM including interface traps, while solid lines do not take interface traps into account.

AQ8

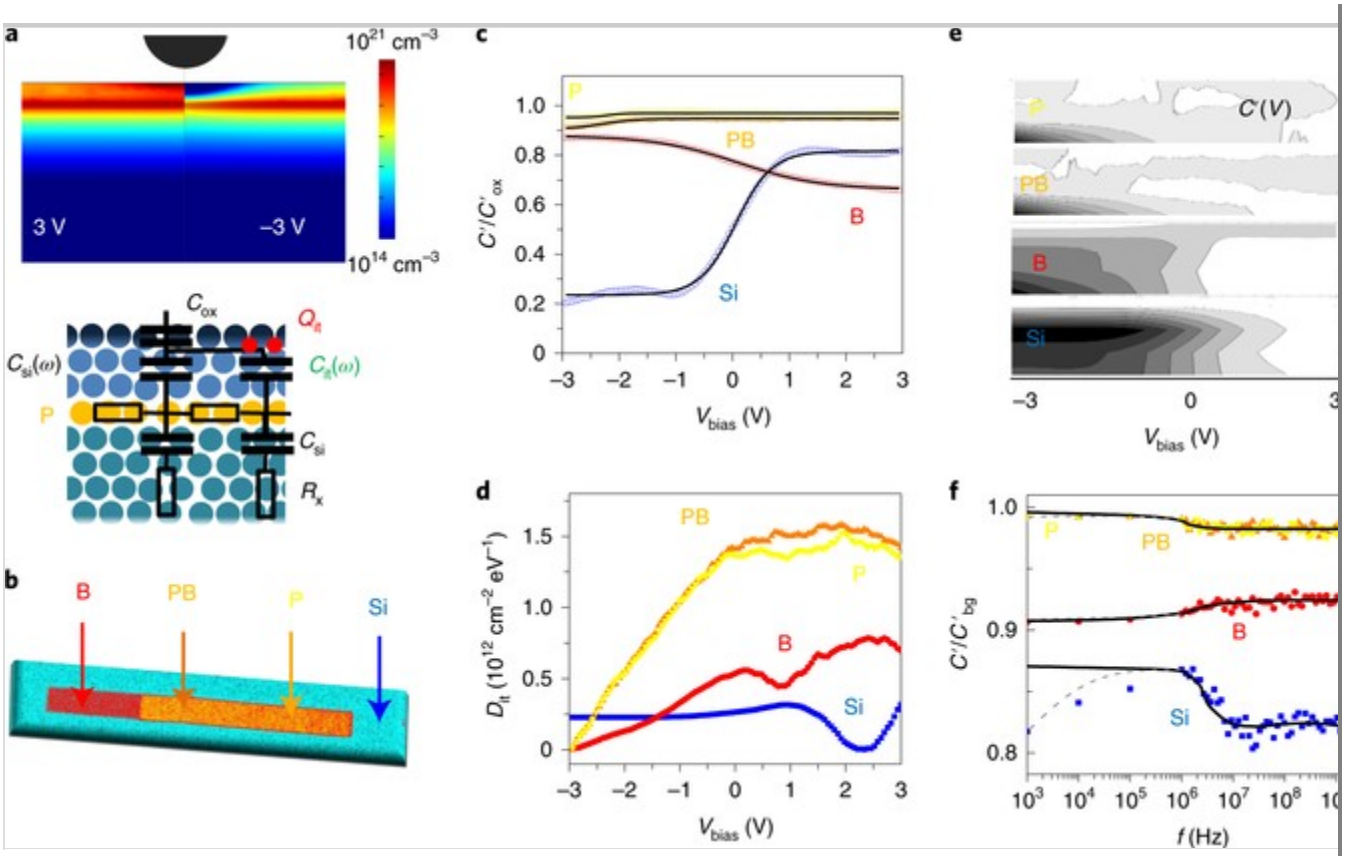

Table 2 displays the results of the δ-layer dopant density and vertical peak position quantification using FEM, as described above. We note that while the P- and B-doped regions show clearly different $C'(V)$ curves, the region containing mixed P and B doping is dominated by the P response and is almost indistinguishable from the pure P region. The n-type (counter)doping seems to completely eradicate the p-type contrast. Although the single-species pattern B and P measured depths h are hardly distinguishable (Table 2), this observation in the mixed-species pattern might be explained by an enhanced segregation of the P atoms towards the surface during Si overgrowth[~~28, 33~~][33] compared to the B atoms. In this way, the P atoms could effectively shield contributions to the response from the B dopants. This is confirmed by the simulated $C'(V)$ curves from different overlapping B and P dopant distribution widths displayed in Extended Data Fig. 9. This hypothesis can be further supported by the SIMS profiles in ref. [7], and would also explain the overall lower signal contrast on B compared to P observed in Fig. 2.

Table 2

Doping profiling results obtained from FEM calculations and experimental data for the P and B sample

	ρ (10^{20} cm^{-3})		h (nm)	
Dopant	$C'(V)$	$C'(z)$	$C'(V)$	$C'(z)$
B	5.8 ± 0.4	5.3 ± 4	15 ± 3	15 ± 0.9
B + P	6.1 ± 0.6	–	13 ± 3	–
P	6.7 ± 0.7	6.1 ± 3	14 ± 2	14 ± 0.8

Results correspond to fits shown in Fig. 4c, with P/B δ-layer at h = 15 nm in Si with a 3 × 10^{15} cm^{-3} As background doped.

AQ9

In addition to determining the carrier type, frequency-dependent C' measurements provide information about imperfections such as oxide-interface charges or interface traps near the surface of the Si. Such imperfections are of great practical significance because they can lead to reductions in semiconductor device performance[14[16]]. Although fixed oxide charges Q_{ox} either repel or attract carriers and thus effectively add to the applied potential in the $C'(V)$ curve, interface traps Q_{it} can trap holes as well as electrons and thus modify the $C'(V)$ spectra in a more complex way[2933[30, 34]]. These interface traps can be effectively modelled as an additional capacitance C_{it} in parallel with the depletion capacitance C_{dep} (Fig. 4a). Because interface traps can only follow low-frequency alternating electric fields[3435], it has been shown by Castagné and Vapaille using standard, on-wafer capacitance voltage spectroscopy[35] that, by comparing high- and low-frequency $C(V)$s, the density of interface states can be successfully extracted following the equation

$$D_{it} = \frac{C_{ox}}{A\,Q}\left(\frac{C_{lf}}{C_{ox} - C_{lf}} - \frac{C_{hf}}{C_{ox} - C_{hf}}\right) \quad (3)$$

where C_{ox} is the oxide capacitance, Q is the elementary charge and C_{lf} and C_{hf} are the low- and high-frequency capacitances, respectively. The term in parenthesis is just a ratio and the capacitance C_{ox} in the first term can be normalized by the area to $c_{ox} = C_{ox}/A$. Thus, we can adapt this equation to our

measurements by exchanging the capacitance variables with our measured capacitance gradient data C' at low and high frequency, respectively:

$$D_{\mathrm{it}} = \frac{c_{\mathrm{ox}}}{Q}\left(\frac{C'_{\mathrm{lf}}}{C'_{\mathrm{lf,ac}} - C'_{\mathrm{lf}}} - \frac{C'_{\mathrm{hf}}}{C'_{\mathrm{hf,ac}} - C'_{\mathrm{hf}}}\right) \quad (4)$$

~~Although~~ While the oxide capacitance in the parentheses corresponds to the capacitance gradient measured in accumulation, C'_{ac}, we calculate the value for c_{ox} assuming an oxide thickness of 2 nm and $\varepsilon_{\mathrm{r}} = 3.8$. In this way, we directly obtain quantitative values of D_{it} from our measurements without the need for FEM. We measured $C'(V)$ curves at four frequencies from 1 kHz to 1 MHz and visualize the signal $C(V,f)$ in Fig. 4e in a contour plot. We use equation (4) to calculate $D_{\mathrm{it}}(V)$ from the high-frequency (100 kHz) and low-frequency (1 kHz) data. Trap densities obtained for Si in this way agree with values typically reported in the literature for native Si/SiO_2 interfaces[36]. For the P δ-layer we observe an increase in D_{it} at positive gate voltages, with a maximum of up to $D_{\mathrm{it}} = 1.5 \times 10^{12}\ \mathrm{cm}^{-2}\ \mathrm{eV}^{-1}$ (Fig. 4d). This higher density of interface traps above the P δ-layer is related to surface segregation of the P dopants, which increase the lattice mismatch and induce the formation of trivalent Si atoms, which act as amphoteric traps[~~29~~[34]]. Interestingly, we observe a significantly lower trap density of $D_{\mathrm{it}} = 0.7 \times 10^{12}\ \mathrm{cm}^{-2}\ \mathrm{eV}^{-1}$ above the B δ-layer, which can again be explained by the lower surface segregation of B compared to P.

AQ10

AQ11

Finally, from $C'(f)$ spectra acquired at 0-V bias at different sample locations (Fig. 4f), we find that the interface traps mainly affect the capacitance data in the low-frequency range below 1 MHz. For frequencies above this value, our $C'(V)$ model, ignoring interface traps, fits well to the data. At lower frequencies we see a clear deviation between model and experiment, especially for Si, where we observe a decay at 1–10 MHz related to the time constant $\tau \approx R_x C_{\mathrm{si}}$. Only when we consider interface trapping, shown with the dashed lines, does our model converge better with the experimental data. This result both confirms the presence of interface traps and demonstrates the strength of bb-EFM in its ability to detect and quantify such traps.

Conclusions

We have shown that bb-EFM can be used to determine both the 3D position and the carrier density of buried dopant nanostructures within a Si wafer. The technique can simultaneously distinguish regions of atomically thin n-type and p-type doping, as well as distinguish trapped charges from mobile carriers induced by dopants and local gating. The technique operates in tapping mode, is non-destructive and allows pinpointing of the lateral and vertical positions of δ-layers with 10-nm and 0.5-nm resolution, respectively. This is a factor of 5 better than the resolution reported previously for SMM[15] and a factor of 10 better than reported for SCM[37] on similar samples. The improved resolution is due to a high electrical sensitivity of 1 pF m^{-1} and the ability to sense the local capacitance gradients across a wide frequency range from 1 kHz to 10 GHz. This allows interface traps in regions containing different dopant types to be identified.

In the devices tested here, the bb-EFM data reveal that there is probably a significant segregation of P towards the surface, whereas the B remains well confined—a fabrication issue that could be solved by growing a locking layer to limit the segregation[38]. When combined with semiconductor FEM for parameter quantification, this approach could be used as a diagnostic imaging tool for the next generation of classical and quantum devices. Furthermore, the ability to detect the insertion of hardware Trojans[1], particularly when implemented below the gate level, would be invaluable for the security sector. It has been shown that by changing the dopant polarity of existing transistors, the cryptographically secure function of certain Intel processors can be compromised[39]. This Trojan could not be detected using optical reverse engineering because only the dopant masks are modified. Although non-destructive X-ray tomography of integrated circuits[3, 4] can provide full 3D images not provided by the bb-EFM (which cannot look underneath metallic screening layers), the X-ray technique is insensitive to the electrons and holes directly responsible for chip functionality. We believe these techniques are complementary and could be used in tandem for non-destructive chip inspection.

Methods

Sample preparation

The 3D phosphorus sample was fabricated in an Omicron VT-STM system with a

base pressure of less than 2×10^{-10} mbar. An n-type (15 Ω cm, 500-µm thickness) As-doped Si(100) wafer with deep etched registration markers was cut into 9×2 mm^2 samples. After a pre-ultrahigh-vacuum chemical clean with acetone and isopropanol, the sample was loaded into vacuum, thermally cleaned and passivated with hydrogen in a standard process[~~39, 40~~][40]. Electrons from an STM tip were used to depassivate a bar-shaped area of 3.5×0.5 µm followed by a saturation dosage of PH_3 (0.09 ~~L~~Langmuir (L)). This results in molecular adsorption of PH_3 exclusively in the hydrogen evacuated region[~~40~~][41]. Subsequently, second (0.003 L) and third (0.002 L) bars were lithographically defined on the surface following the same procedure. The three bars with locally different dopant densities were encapsulated with 5 nm of Si by molecular beam epitaxy from a Si sublimation source. Si growth included a so-called locking layer technique[~~37~~][38] that was developed to reduce P dopant segregation. Following this process, the first 10 monolayers of the sample were grown at a low sample temperature of ~60 °C. A subsequent short rapid thermal anneal of 15 s at 500 °C incorporated the P atoms into the surface[~~31~~][32], making them electrically active. For further Si growth, the sample temperature was kept at 250 °C. A constant deposition rate of one monolayer per minute was used throughout. After reaching the final thickness, a 2-min anneal to 450 °C flattened the surface, making it suitable for high-quality hydrogen passivation and subsequent lithography steps. The three bars in the top layer were patterned and dosed with the same parameters as the bottom layer bars, but rotated by 90°.

AQ12

The combined B and P sample was prepared on a Si(100) wafer (1.5 Ω cm, 500-µm thickness). The Si surface was cleaned, then passivated with hydrogen in ultrahigh vacuum, using a standard process[~~39~~][40]. Patterns of clean Si were written by depassivating the Si(100)-2 × 1:H surface[~~41~~][42] using the electron beam from an STM tip, as for the other sample, above. The patterned surface was first exposed to a background PH_3 pressure of $\sim 1 \times 10^{-9}$ mbar for 2 min, which resulted in adsorption of the PH_3 molecules exclusively within the depassivated regions[~~40~~][41]. Subsequently, the STM was used again to depassivate an additional region, which was then exposed to a background B_2H_6 pressure of $\sim 1 \times 10^{-9}$ mbar again for 2 min. The P and B atoms were incorporated into the surface via a 2-min anneal at 350 °C (ref. [~~26~~][32]) and subsequently the donor nanostructure was encapsulated with 15 nm of silicon, grown by molecular beam

epitaxy from a Si sublimation source. A low sample temperature of ~250 °C during Si sublimation provided both low donor surface segregation and relatively smooth Si crystal growth[42][43]. Further details on sample preparation are provided in ref. [7].

Experimental set-up

The experimental set-up for 3D dopant profiling is shown in Fig. 1 and consists of a 5600 AFM (Keysight Technologies) operated in tapping mode and interfaced with a signal generator through a coaxial cable and tip holder capable of delivering high-frequency signals up to the tip (SMM nose cone). Additionally, a bias voltage can be applied to the tip or the substrate. We used a MXG5183B analog signal generator to cover a frequency range from 1 kHz to 10 GHz. A sinusoidal voltage signal with an angular frequency f_{carrier} was applied between a conductive probe and the bottom of the sample, and the force in equation (1) was measured.

We found that PtSi-FM cantilevers (Nanosensors) with a nominal spring constant of 2.8 N m^{-1} and a resonance frequency of 67 kHz offered the best trade-off among mechanical stability, wear resistance and electrical conductivity. We also tested highly doped Si and diamond probes (Nanosensors), standard Pt-coated Si probes (Nanosensors) and full Pt probes (RMN). The first two tips showed too low conductivity at frequencies above a few MHz, and the full Pt tips did not allow for stable tapping-mode imaging at low amplitudes. The standard Pt-coated tips tended to wear off and modify very quickly, which is disadvantageous for calibration. When the carrier frequency was beyond the mechanical resonance of the cantilever, the cantilever continued to bend statically due to the nonlinear dependence of the actuation force on the applied voltage. Amplitude modulation of the carrier at a low frequency, f_{mod}, of ~1 kHz led to an oscillation of the down-modulated force, which was detected with an enhanced SNR by a lock-in amplifier sensing directly at the modulation frequency f_{mod} or by demodulating the phase shift of the mechanical cantilever oscillation at f_{mod}.

Frequency calibration was carried out as in ref. [43][44]. In short, an image was acquired on the region of interest in lift mode at three different lift heights from the surface (for example, 20 nm, 30 nm and 50 nm). Although While the x-scan was active, the y-scan was stopped and the measurement frequency was changed

at every new line, producing a frequency spectrum for every lift height. Extrapolation of the scanning distance defined the background of the frequency spectrum, which was used to normalize the data. Measurements were carried out in a dry nitrogen atmosphere.

FEM

FEM was carried out with COMSOL Multiphysics 5.4 (2D axisymmetric, electrostatics + semiconductor module, semiconductor equilibrium, frequency domain perturbation). The simulation geometry for quantification resembled the experimental conditions. The model consisted of a 15-µm-high AFM tip modelled as a truncated cone with a cone angle θ and cantilever extending the cone end by 10 µm. The tip had a spherical apex with radius R and was located at a distance z above the sample. The sample comprised a 250-µm-thick Si substrate (we verified that the exact thickness is not relevant for our calculations) with a constant background doping of 3×10^{14} cm^{-3} and 3×10^{15} cm^{-3} for the two different samples, respectively. The additionally grown 15-nm-thick Si layer on the surface was modelled as being undoped. The P and B δ-layers were modelled as acceptor and donor doping distributions with a Gaussian shape centred at h nm below the surface with $\sigma = 1.5$ nm, and a lateral width corresponding to the area of the patterned δ-layer. To account for the segregation of dopants towards the surface, we modelled the region between tip and doping layer with a doping density 10 times smaller than the peak value of the δ-layer. The probe surrounding was air with the same size as the Si region. Fermi–Dirac statistics were used to obtain the correct results for high dopant concentrations. The available mobility models—Arora and Fletcher Models—were implemented. A Shockley–Read–Hall generation recombination model was used. To achieve accurate results and convergence of the solution, the meshing was set to scale with the size of the involved geometries. In this way the mesh size on the boundary of the apex and membrane was always at least 20 times smaller than the tip apex. The model was meshed from the inside (apex + δ-layer region) to the outside (cone and surrounding area). Outside parts were meshed automatically by Comsol. The downward directed Maxwell stress tensor in z direction was calculated from the small-signal solution on the tip boundaries, which had been set to Terminal. From these data the capacitance gradient was calculated. To determine the tip geometry, a combination of experiments and simulations were carried out[~~1~~3~~1~~44]. Electrostatic force approach curves (z from 2

to 500 nm) were simulated for a wide range of tip radii R and cone angle θ. Using a fitting procedure with the simulated approach curves, we extracted the tip radius and cone angle that led to the best agreement with the experimental approach curve[45].

AQ13

AQ14

After estimation of the tip geometry, the capacitance gradient C' was calculated for a wide range of dopant concentrations ρ and depth h, changing the measurement parameters (bias V, frequency f and tip–sample distance z, respectively) while keeping the geometry fixed. A look-up table/interpolation function was generated from these data to fit the simulated data to the experimental data. The fitting results are ρ and depth h. Note that the calculated forces from the small-signal solution assume small a.c. voltages of <1 V to satisfy the harmonic perturbation approach. To relate experiments obtained at excitation voltages of 2–3 V with the simulations, an additional integration–differentiation step over the experimental voltage range was necessary.

Extended data is available for this paper at https://doi.org/10.1038/s41928-020-0450-8.

Supplementary information is available for this paper at https://doi.org/10.1038/s41928-020-0450-8.

Publisher's note Springer Nature remains neutral with regard to jurisdictional claims in published maps and institutional affiliations.

Acknowledgements

Technical discussions with I. Alic are acknowledged. This work has been supported by FWF project no. P28018-B27, EFRE project no. IWB 2018 98292, NMBP project no. MMAMA 761036 and UKRI EPSRC project no. EP/M009564/1.

Author contributions

G.G. conceived and designed the experiments, performed the experiments, analysed the data and wrote the paper. A.K. performed the experiments, contributed materials/analysis tools and wrote the paper. T.S. contributed materials/analysis tools and wrote the paper. T.J.Z.S. wrote the paper. G.A.

conceived and designed the experiments and wrote the paper. F.K. conceived and designed the experiments. A.F. contributed materials/analysis tools, conceived and designed the experiments and wrote the paper. N.J.C. conceived and designed the experiments and wrote the paper.

AQ15

Data availability

All data needed to evaluate the conclusions in this paper are present in the paper and/or the Supplementary Information. Additional data related to this paper can be requested from the authors. The data created during this research are available at https://doi.org/10.5281/zenodo.3899692.

Competing interests The authors declare no competing interests.

Extended data

Extended Data Fig. 1

STM images of patterned Si surface.

STM images of patterned Si surface prior to coverage with Si. **a**, Layout of patterns at which hydrogen is desorbed on the Si surface. **b**, **c**, Zoom and overview STM image of boron pattern imaged before coverage with Si. Actual width of stripes appears to be 6 nm, 10 nm, 19 nm, 35 nm, with a pitch of 9 nm. The error between design and measured width is due to finite desorption width of the hydrogen.

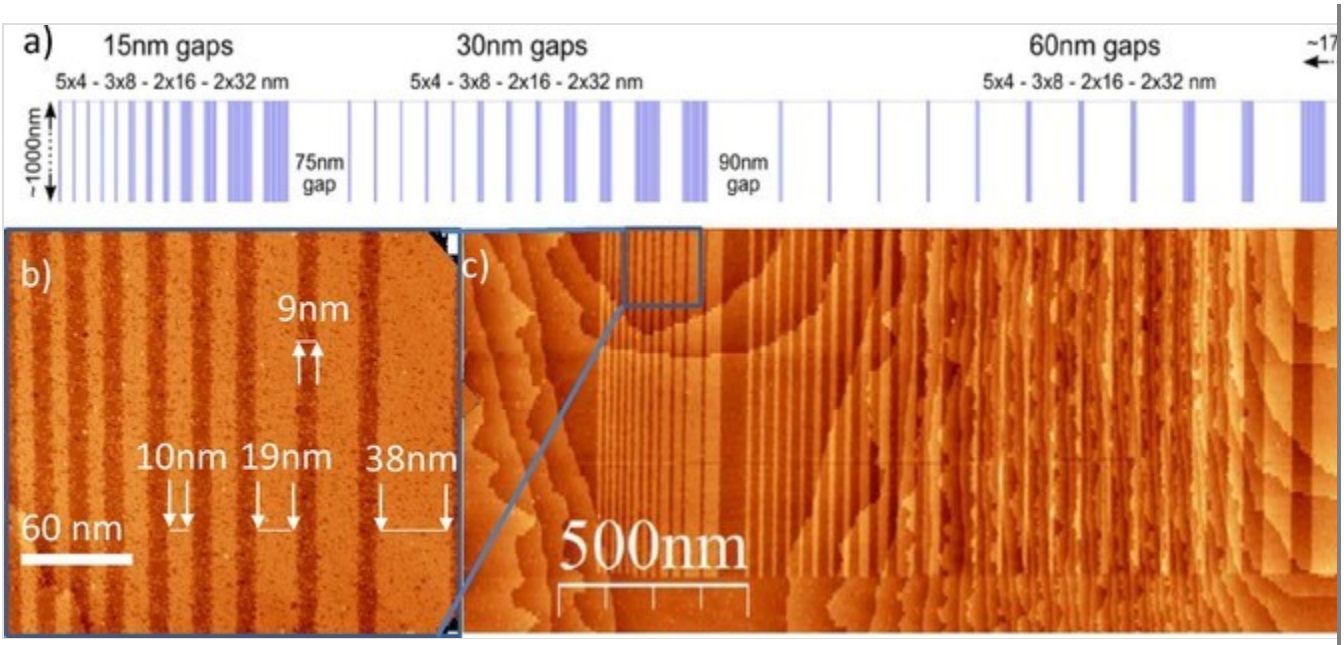

Extended Data Fig. 2

EFM image after 2 h of continuous scanning and tip calibration.

EFM image after 2 h of continuous scanning with the PtSi tip and tip calibration. **a**, Zoom onto the stripes separated by 100 nm, 70 nm and 30 nm, **b**, corresponding line profile as indicated. PtSi-FM tips from Nanonsensors (Germany) with nominal tip radius 20–30 nm were used. At the end of the measurement the tip was calibrated by approach curve **c**, *C'(z)* approach curve for tip calibration as detailed in the methods section. Black dots for fresh tip. Red dots after prolonged scanning. Blue line represents simulated curve that fits best to the experimental data with a tip radius of $r_a = 26.4 \pm 0.2$ nm and $r_a = 31.2 \pm 0.3$ nm for fresh and worn tip, respectively.

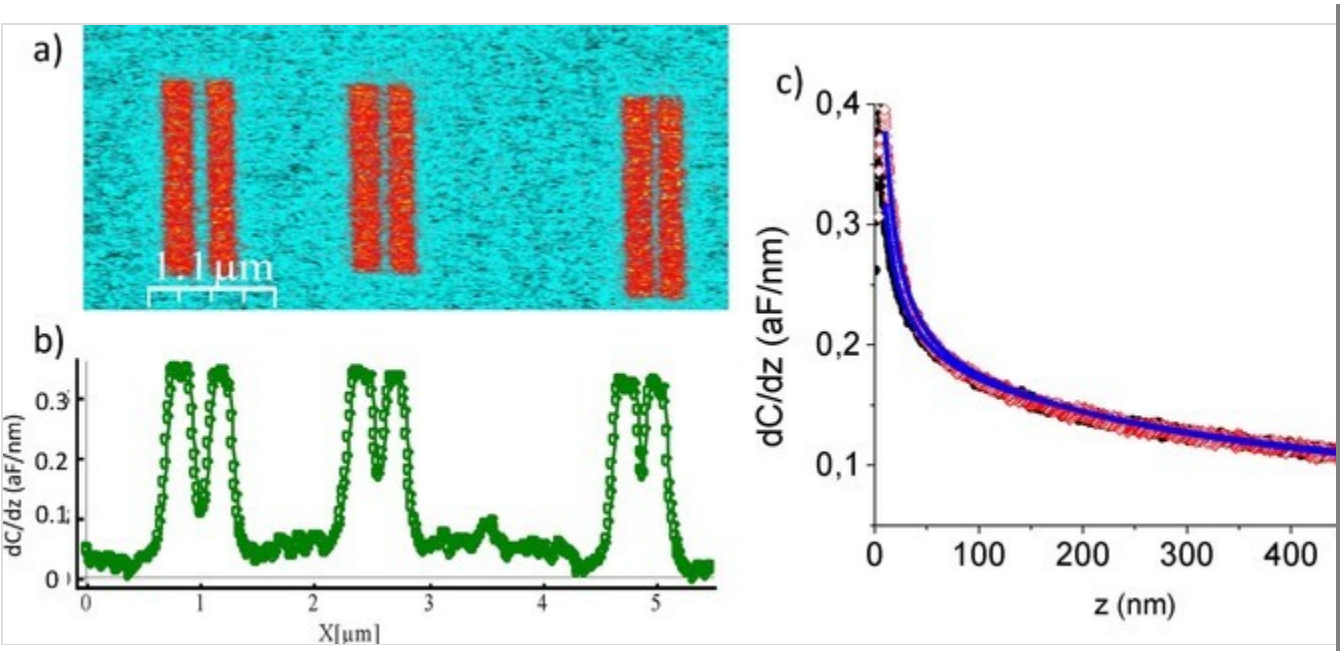

Extended Data Fig. 3

Comparison of SMM and EFM lateral resolution.

Comparison of SMM and EFM lateral resolution. **a**, EFM *C'* image of P δ-layer stripes buried 15 nm below the surface and **b**, corresponding line profile as indicated in the image. A fresh PtSi-FM tip from Nanonsensors (Germany) with calibrated tip radius of $r_{a,EFM} = 26.4 \pm 0.2$ nm was used. Peaks were fitted with two double logistic functions (solid lines) giving a lateral resolution of 13 ± 2 nm and 10 ± 1 nm for first and second peak, respectively. **c**, SMM capacitance image and **d**, corresponding profile line as reported in Gramse et al[~~13~~[15]]. Solid Pt tips from (RMN, US) were used and tip radius was calibrated to be $r_{a,SMM} = 20$ nm). The scan-rate in both images was identical with 0.4 lines per second.

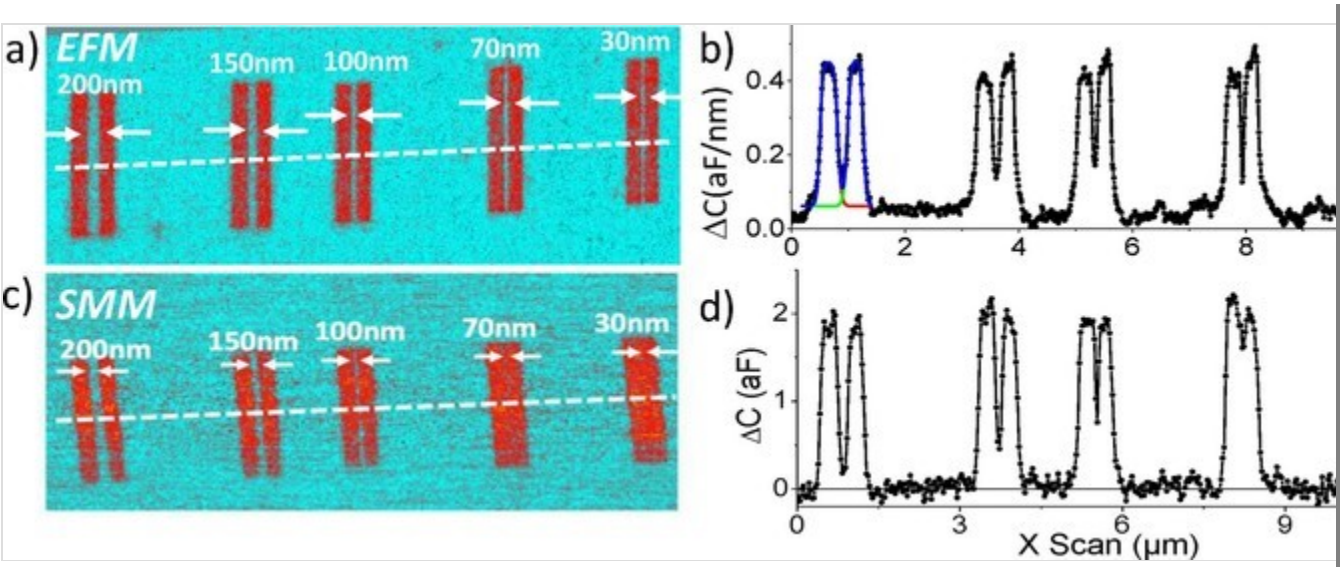

Extended Data Fig. 4

Comparison of lateral resolution in current and force-sensing techniques.

Comparison of lateral resolution in current and force-sensing techniques and impact of measurement parameters. Dashed lines represent modelled *C(z)* scan line and solid lines *C'(z)* scan line over a 500 nm wide stripe of phosphorus. Effect of tip radius, tip–sample distance and carrier frequency are studied as indicated, while the other parameters are fixed to $R = 16$ nm, $z = 21$ nm, $f = 1$ MHz.

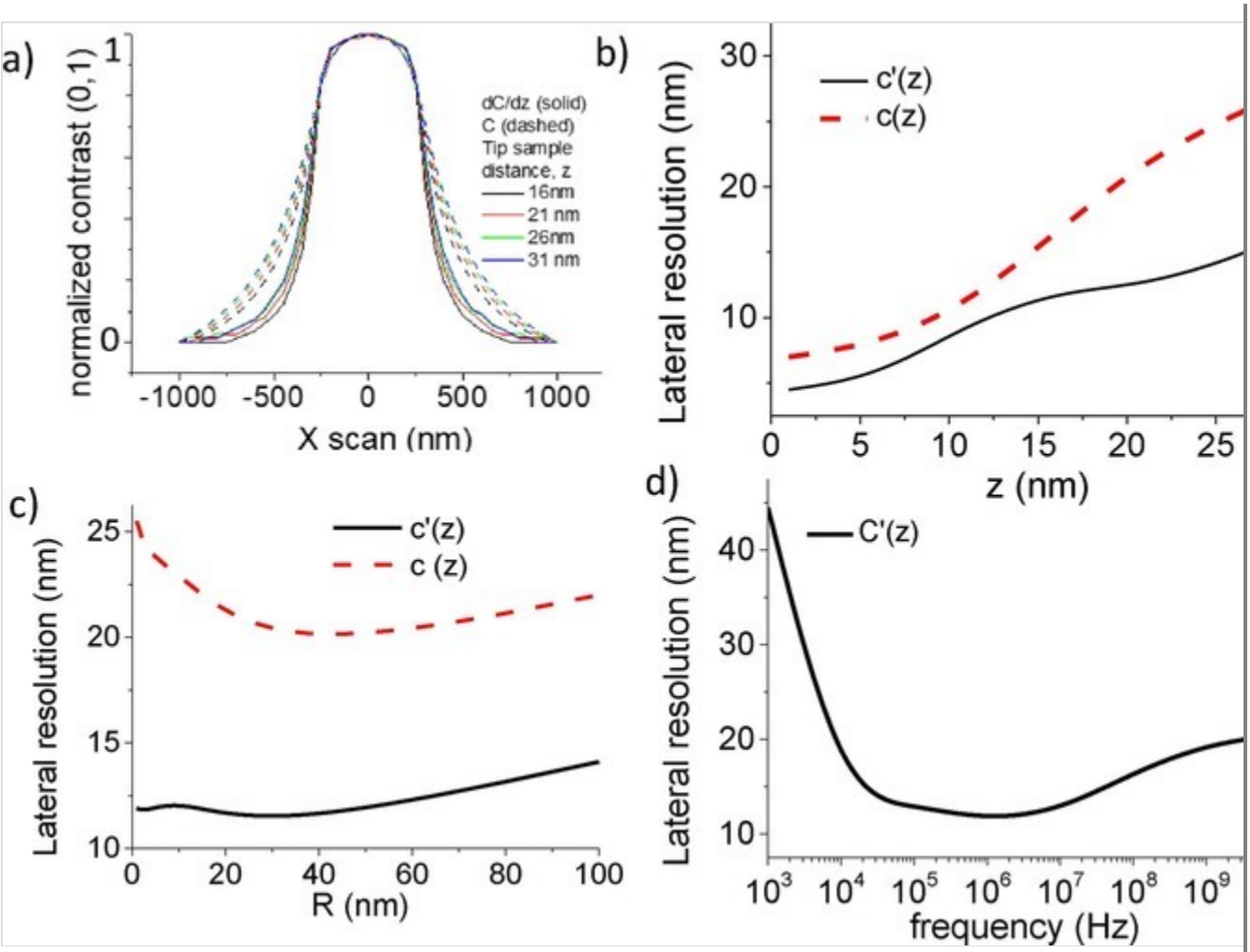

Extended Data Fig. 5

Experimental comparison of EFM lateral resolution and electrical contrast at different frequencies.

Experimental comparison of EFM lateral resolution and electrical contrast on dopant test sample measured at different frequencies. Histograms are shown as black insets. We found best contrast at measurement frequencies of ~~between~~ 10–100 MHz ~~measurement frequency~~ as can be seen in the insets.

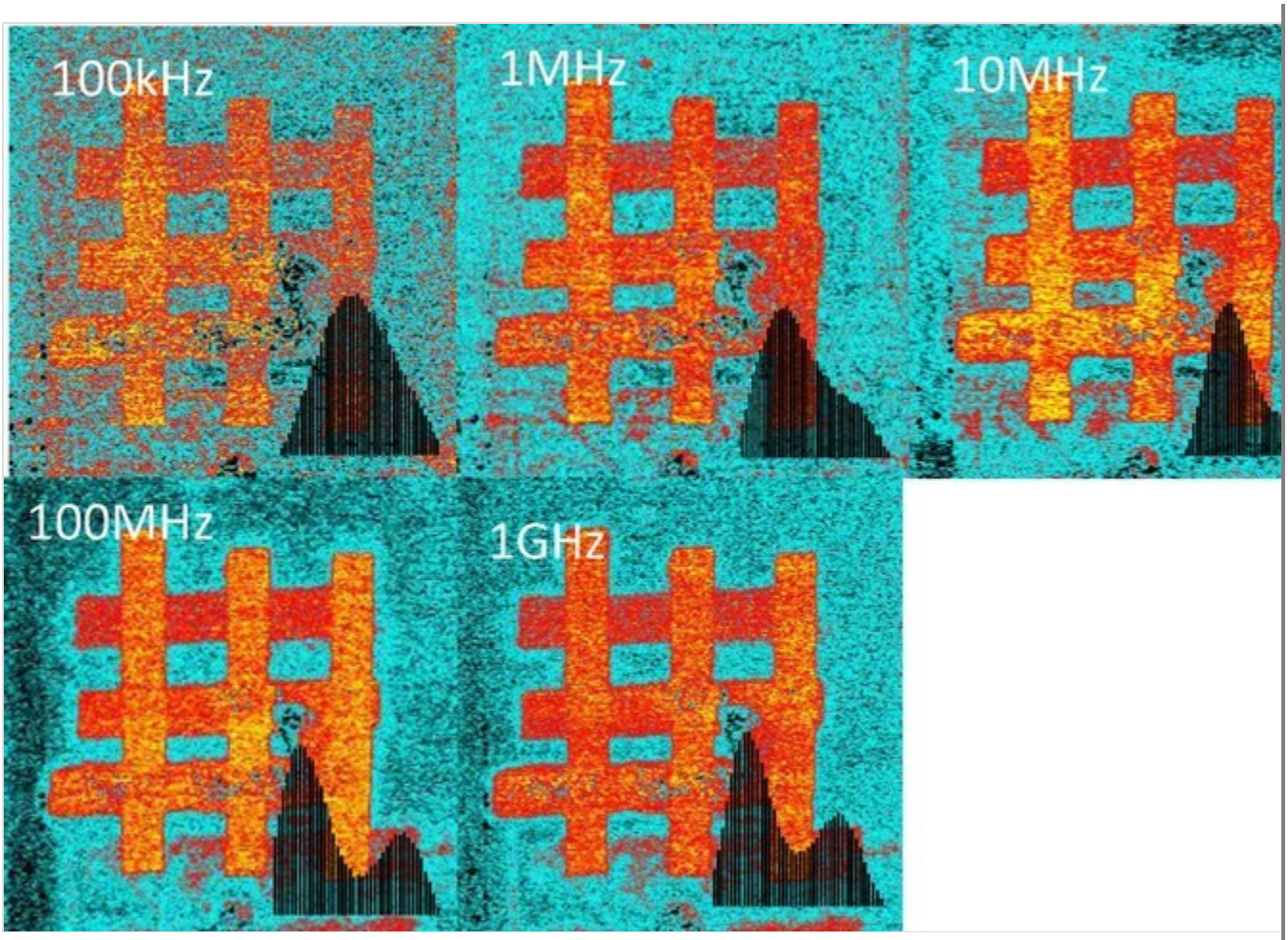

Extended Data Fig. 6

Simulated carrier profile and capacitance bias curve.

Simulated carrier profile and capacitance bias curve. **a**, Calculated carrier concentration (phosphorus doping) below the tip (along the symmetry axis) for various applied voltages for dopant concentration $3\times10^{21}cm^{-3}$ (orange) and $3\times10^{18}cm^{-3}$ (red). **b**, Corresponding simulated *C'(V)* curve.

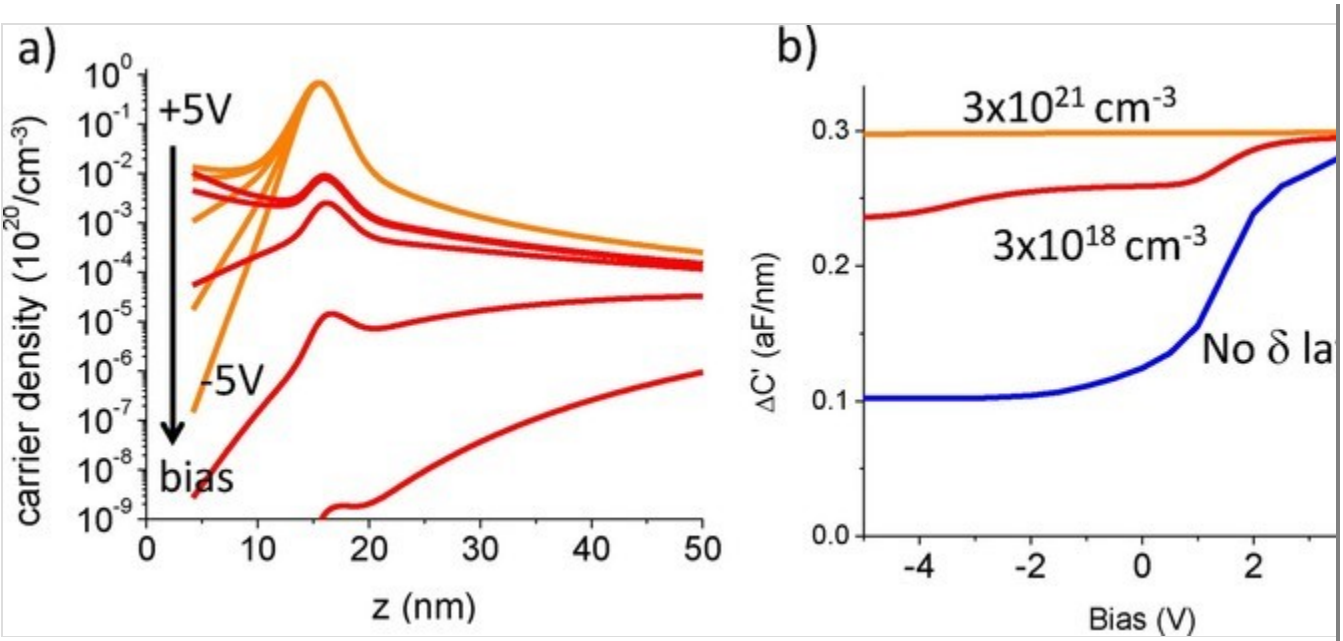

Extended Data Fig. 7

Sensitivity analysis to amount of dopants and lateral resolution.

Sensitivity analysis to amount of dopants and lateral resolution. **a**, Solid line represents calculated contrast of acceptor dopant delta layer with radius r = 20 µm at 15 nm below the surface as a function of dopant density. Dashed lines show the same for donor doping and varying delta layer radii. The EFM electrical sensitivity is ~1zF/nm for the here used tips (area is marked), it can be improved to 0.3zF/nm using softer tips. **b**, Lateral resolution as a function of delta layer dopant concentration (other parameters are fixed to h = 15 nm, R = 16 nm, z = 21 nm, f = 1 MHz).

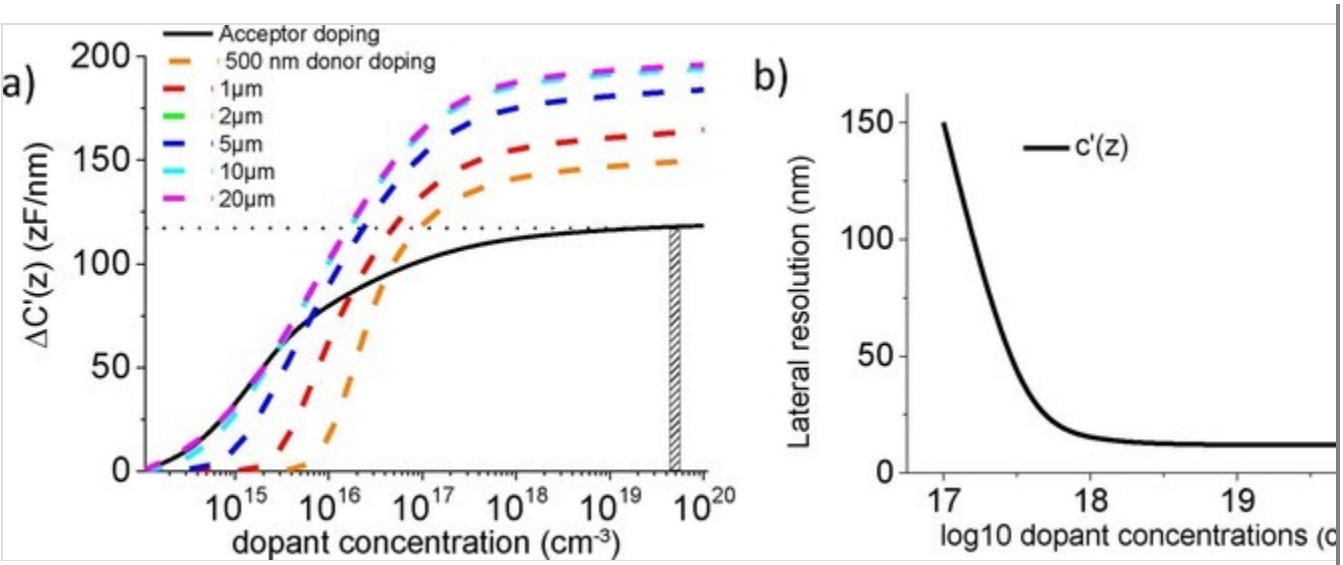

Extended Data Fig. 8

2D Finite element model for estimation of the measurement parameters.

2D Finite element model for estimation of the measurement parameters on the lateral resolution. Shown is the electron concentration in the substrate. A 500 nm wide stripe of highly doped phosphorus (3×10^{20} cm^{-3}) at a depth of 15 nm is moved below the probe. Capacitance and Maxwell-Stress Tensor are calculated.

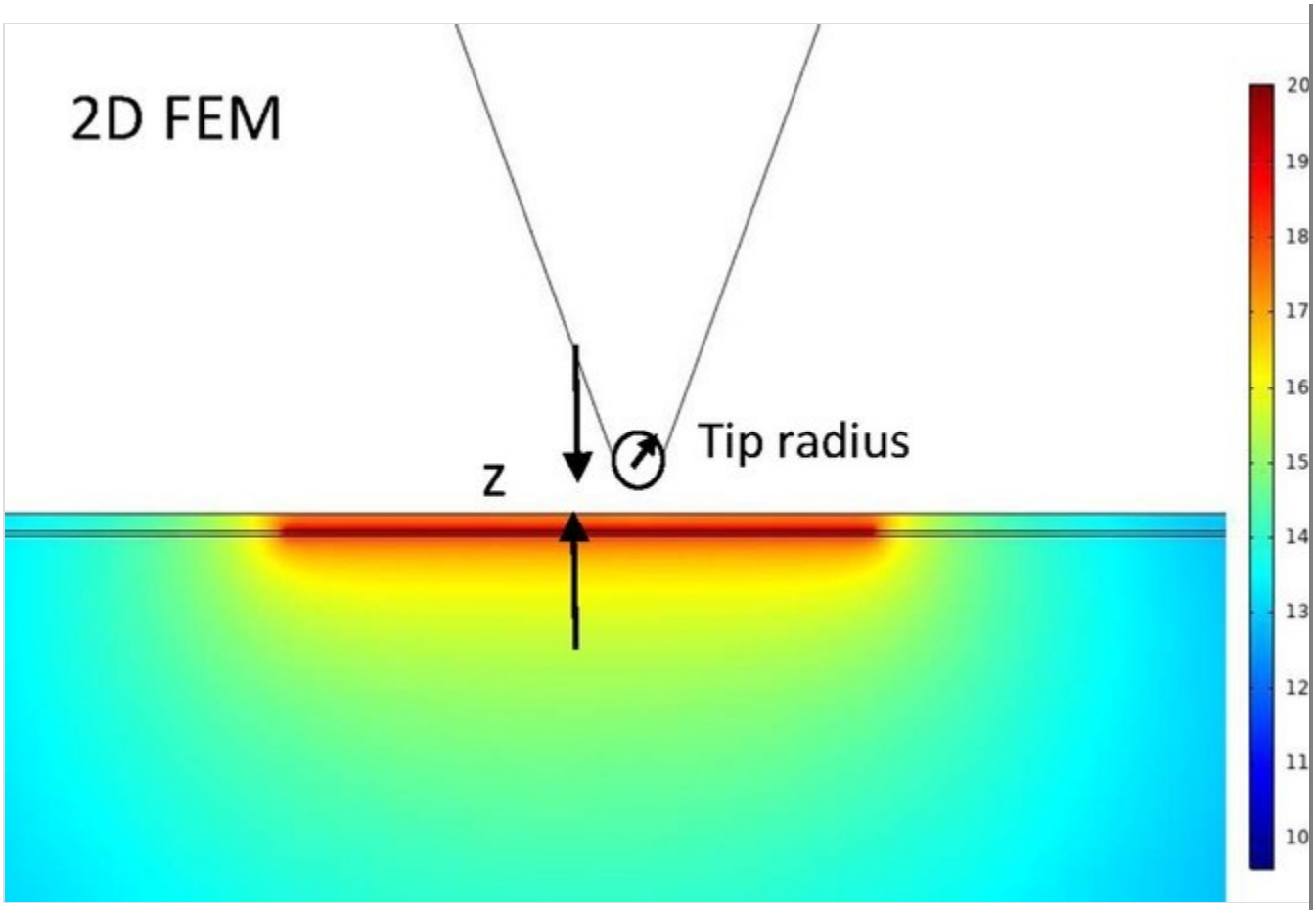

Extended Data Fig. 9

Simulated capacitance bias curve for different doping profiles.

Simulated capacitance bias curve for different doping profiles. **a**, Simulated doping profile below the tip for P, B and mixed P + B doping layers as indicated in the plot **b**, Corresponding simulated *C'(V)* curve.

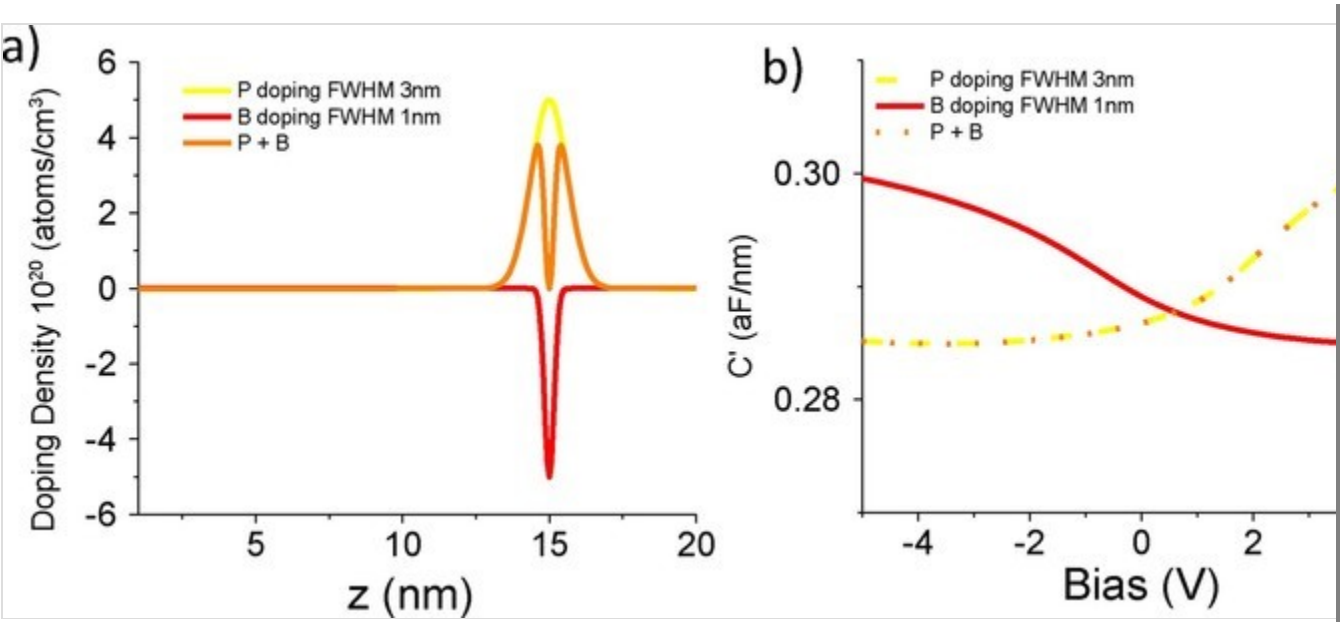

Extended Data Fig. 10

Single *C'(V)* spectra from Fig. 4c.

Single *C'(V)* spectra that were averaged Fig. 4c). Curves show good reproducibility as long as the tip is not modified.

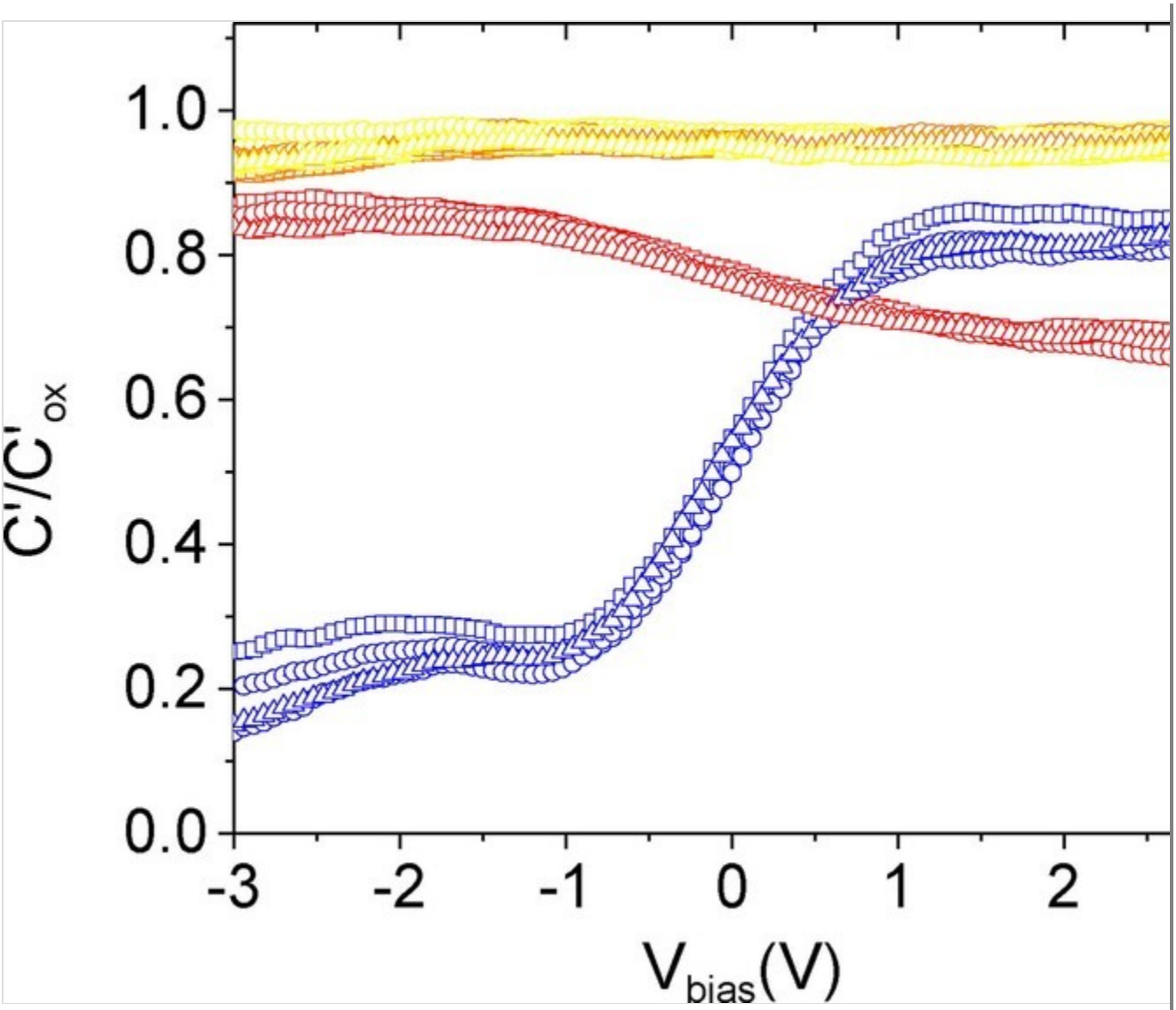

Supplementary information

Supplementary Information

Supplementary discussion and Figs. 1 and 2.

References

1. Yang, K. H. M., Dong, Q., Austin, T. & Sylvester, D. Analog malicious hardware. In *Proceedings of 2016 IEEE Symposium on Security and Privacy* 18–37 (IEEE, 2016).

AQ16

2. Orji, N. G. et al. Metrology for the next generation of semiconductor devices. *Nat. Electron.* **1**, 532–547 (2018).

3. Holler, M. et al. Three-dimensional imaging of integrated circuits with macro- to nanoscale zoom. *Nat. Electron.* **2**, 464–470 (2019).

4. Holler, M. et al. High-resolution non-destructive three-dimensional imaging of integrated circuits. *Nature* **543**, 402–406 (2017).

5. Zschech, E. & Diebold, A. Metrology and failure analysis for 3D IC integration. *AIP Conf. Proc.* **1395**, 233–239 (2011).

6. Hill, C. D. et al. A surface code quantum computer in silicon. *Sci. Adv.* **1**, e1500707 (2015).

7. Škereň, T., Köster, S., Douhard, B., Fleischmann, C. & Fuhrer, A. Bipolar device fabrication using a scanning tunneling microscope. *Nat. Electron.* (in the press); https://doi.org/10.5281/zenodo.3881492

8. Stock, T. J. Z. et al. Atomic-scale patterning of arsenic in silicon by scanning tunneling microscopy. *ACS Nano* **14**, 3316–3327 (2020).

9. Goh, K. E. J., Oberbeck, L., Simmons, M. Y., Hamilton, A. R. & Butcher, M. J. Influence of doping density on electronic transport in degenerate Si:P δ-doped layers. *Phys. Rev. B* **73**, 035401 (2006).

10. Ruess, F. J. et al. Toward atomic-scale device fabrication in silicon using scanning probe microscopy. *Nano Lett.* **4**, 1969–1973 (2004).

11. Buech, H., Fuechsle, M., Baker, W., House, M. G. & Simmons, M. Y. Quantum dot spectroscopy using a single phosphorus donor. *Phys. Rev. B* **92**, 235309 (2015).

12. Koch, M. et al. Spin read-out in atomic qubits in an all-epitaxial three-dimensional transistor. *Nat. Nanotechnol.* **14**, 137–140 (2019).

13. *International Technology Roadmap for Semiconductors—ITRS 2.0* (ITRS, 2015); http://www.itrs2.net

14. Oberbeck, L. et al. Imaging of buried phosphorus nanostructures in silicon using scanning tunneling microscopy. *Appl. Phys. Lett.* **104**, 253102 (2014).

15. Gramse, G. et al. Nondestructive imaging of atomically thin nanostructures buried in silicon. *Sci. Adv.* **3**, e1602586 (2017).

16. Cheng, B., Roy, S., Roy, G., Adamu-Lema, F. & Asenov, A. Impact of intrinsic parameter fluctuations in decanano MOSFETs on yield and functionality of SRAM cells. *Solid State Electron.* **49**, 740–746 (2005).

17. Holmberg, V. C., Helps, J. R., Mkhoyan, K. A. & Norris, D. J. Imaging impurities in semiconductor nanostructures. *Chem. Mater.* **25**, 1332–1350 (2013).

18. Lenk, A., Lichte, H. & Muehle, U. 2D-mapping of dopant distribution in deep sub micron CMOS devices by electron holography using adapted FIB-preparation. *J. Electron Microsc.* **54**, 351–359 (2005).

19. Zalm, P. C. Ultra-shallow doping profiling with SIMS. *Rep. Prog. Phys.* **58**, 1321–1374 (1995).

20. De Wolf, P., Snauwaert, J., Clarysse, T., Vandervorst, W. & Hellemans, L. Characterization of a point-contact on silicon using force microscopy-supported resistance measurements. *Appl. Phys. Lett.* **66**, 1530–1532 (1995).

21. Gramse, G., Edwards, M. A., Fumagalli, L. & Gomila, G. Theory of amplitude modulated electrostatic force microscopy for dielectric measurements in liquids at MHz frequencies. *Nanotechnology* **24**, 415709 (2013).

22. Fumagalli, L. et al. Nanoscale capacitance imaging with attofarad resolution using a.c. current sensing atomic force microscopy. *Nanotechnology* **17**, 4581–4587 (2006).

23. Shao, R., Kalinin, S. V. & Bonnell, D. A. Local impedance imaging and spectroscopy of polycrystalline ZnO using contact atomic force microscopy. *Appl. Phys. Lett.* **82**, 1869–1871 (2003).

24. Lányi, S. & Hruskovic, M. The resolution limit of scanning capacitance microscopes. *J. Phys. D* **36**, 598 (2003).

25. Cho, Y. et al. Scanning nonlinear dielectric microscopy with nanometer resolution. *Appl. Phys. Lett.* **75**, 2833–2855 (1999).

26. Gramse, G. et al. Quantitative sub-surface and non-contact imaging using scanning microwave microscopy. *Nanotechnology* **26**, 135701 (2015).

27. Gil, A., Colchero, J., Gomez-Herrero, J. & Baro, A. M. Electrostatic force gradient signal: resolution enhancement in electrostatic force microscopy and improved kelvin probe microscopy. *Nanotechnology* **14**, 332–340 (2003).

28. Girard, P. & Titkov, A. N. *Applied Scanning Probe Methods II*: *Scanning Probe Microscopy Techniques* Ch. 9.4.3 (Springer, 2006).

29. Girard, P. Electrostatic force microscopy: principles and some applications to semiconductors. *Nanotechnology* **12**, 485–490 (2001).

30. Sze, S. M. & Ng, K. K. *Physics of Semiconductor Devices* 3rd edn (Wiley, 2006)

31. Niranjan, M. K., Zollner, S., Kleinman, L. & Demkov, A. A. Theoretical investigation of PtSi surface energies and work functions. *Phys. Rev. B* **73**, 195332 (2006).

32. Oberbeck, L. et al. Encapsulation of phosphorus dopants in silicon for the fabrication of a quantum computer. *Appl. Phys. Lett.* **81**, 3197–3199 (2002).

33. Polley, C. M. et al. Exploring the limits of n-type ultra-shallow junction formation. *ACS Nano* **7**, 5499–5505 (2013).

34. Schmidt, V., Wittemann, J. V., Senz, S. & Gösele, U. Silicon nanowires: a

review on aspects of their growth and their electrical properties. *Adv. Mater.* **21**, 2681–2702 (2009).

35. Castagné, R. & Vapaille, A. Description of the SiO_2:Si interface properties by means of very low frequency MOS capacitance measurements. *Surf. Sci.* **28**, 157–193 (1971).

36. Mizsei, J. Determination of SiO_2–Si interface trap level density (D_{it}) by vibrating capacitor method. *Solid State Electron.* **44**, 1825–1831 (2000).

37. Bussmann, E. et al. Scanning capacitance microscopy registration of buried atomic-precision donor devices. *Nanotechnology* **26**, 085701 (2015).

38. Keizer, K. G., Koelling, S., Koenraad, P. M. & Simmons, M. Y. Suppressing segregation in highly phosphorus doped silicon monolayers. *ACS Nano* **9**, 12537–12541 (2015).

39. Becker, G. T., Regazzoni, F., Paar, C. & Burleson, W. P. Stealthy dopant-level hardware Trojans: extended version. *J. Cryptographic Eng.* **4**, 19–31 (2014).

40. O'Brien, J. L. et al. Towards the fabrication of phosphorus qubits for a silicon quantum computer. *Phys. Rev. B* **64**, 161401 (2001).

41. Shen, T. C. et al. Ultradense phosphorous δ-layers grown into silicon from PH_3 molecular precursors. *Appl. Phys. Lett.* **80**, 1580–1582 (2002).

42. Adams, D. P., Mayer, T. M. & Swartzentruber, B. S. Nanometer-scale lithography on Si(001) using adsorbed H as an atomic layer resist. *J. Vac. Sci. Technol. B* **14**, 1642–1649 (1996).

43. McKibbin, S. R., Clarke, W. R., Fuhrer, A., Reusch, T. C. G. & Simmons, M. Y. Investigating the regrowth surface of Si:P δ-layers toward vertically stacked three dimensional devices. *Appl. Phys. Lett.* **95**, 233111 (2009).

44. Gramse, G., Schönhals, A. & Kienberger, F. Nanoscale dipole dynamics of protein membranes studied by broadband dielectric microscopy. *Nanoscale*

11, 4303–4309 (2019).

45. Fumagalli, L., Gramse, G., Esteban-Ferrer, D., Edwards, M. A. & Gomila, G. Quantifying the dielectric constant of thick insulators using electrostatic force microscopy. *Appl. Phys. Lett.* **96**, 183107 (2010).